

PAPER • OPEN ACCESS

Goos–Hänchen shift for coupled vibrational modes in a semiconductor structure





To cite this article: Diosdado Villegas *et al* 2024 *J. Phys.: Condens. Matter* **36** 325301

View the [article online](#) for updates and enhancements.

You may also like

- [Precise magnetization measurements down to 500 mK using a miniature \$^3\text{He}\$ cryostat and a closed-cycle \$^3\text{He}\$ gas handling system installed in a SQUID magnetometer without continuous-cooling functionality](#)
Kazutoshi Shimamura, Hiroki Wajima, Hayato Makino et al.
- [Global anthropogenic emissions in urban areas: patterns, trends, and challenges](#)
Monica Crippa, Diego Guizzardi, Enrico Pisoni et al.
- [Influence of orbital angular momentum of vortex light on lateral shift behavior](#)
Saeed Ahmad, Muqaddar Abbas, Muhammad Awais et al.

Goos–Hänchen shift for coupled vibrational modes in a semiconductor structure

Diosdado Villegas^{1,2}, Zorayda Lazcano^{2,*} , Jesús Arriaga² , R Pérez-Álvarez³ 
and Fernando de León-Pérez^{4,*} 

¹ Departamento de Física, Universidad Central ‘Marta Abreu’ de Las Villas, Santa Clara, Cuba

² Instituto de Física, Benemérita Universidad Autónoma de Puebla, CP 72570 Puebla, Mexico

³ Instituto de Investigación en Ciencias Básicas y Aplicadas (IICBA), Universidad Autónoma del Estado de Morelos, Av. Universidad 1001, CP 62209 Cuernavaca, Morelos, Mexico

⁴ Instituto de Nanociencia y Materiales de Aragón (INMA) and Departamento de Física de la Materia Condensada, CSIC-Universidad de Zaragoza, E- 50009 Zaragoza, Spain

E-mail: zlazcano@ifuap.buap.mx and fdlp@unizar.es

Received 18 December 2023, revised 26 February 2024

Accepted for publication 13 March 2024

Published 16 May 2024



CrossMark

Abstract

We present a theoretical investigation of the Goös–Hanchen shift (GHS) experienced by acoustic and optical vibrational modes reflected and transmitted from the surfaces of a semiconductor thin film sandwiched between two semi-infinite media. Our study focuses on the impact of the incident angle on the GHS, considering the coupling between longitudinal and transverse modes. For acoustic vibrations, our findings reveal that the GHS can reach magnitudes up to seven times larger than the thickness of the thin film and up to 20 times larger than the incident wavelength. Besides, it is shown that this significant amplification of the GHS highlights the strong influence of the incident angle and the frequency of the modes involved. In the case of optical vibrations, we observe even more pronounced GHS values, exceeding 30 times the incident wavelength. This demonstrates the potential of GHS in acoustical systems, which opens up possibilities for applications in the design of acoustic devices.

Keywords: Goos–Hänchen shift, vibrational waves, coupled modes, semiconductor structures

1. Introduction

The behaviour of optical, acoustic, and matter waves can be described by solving a wave equation with corresponding boundary conditions. Despite their differences, wave phenomena exhibit similar characteristics. For instance, many of the properties observed in geometrical optics also manifest themselves in acoustic and matter waves. One of such properties is

the reflection of a wave from an interface at an angle of incidence close to the critical value, resulting in a lateral shift of the reflected wave. This phenomenon is known as the Goös–Hänchen effect [1].

The Goös–Hanchen shift (GHS) has recently achieved significant interest due to its potential applications, such as optical differential operations and image edge detection [2], as well as refractive index sensors [3] and plasmonic biosensors [4]. For example, biosensor applications include the design of a structure based on two-dimensional graphene and transition metal dichalcogenides to greatly enhance the GHS, improving the performance of plasmonic biosensors [5]. Additionally, high sensitive label-free optical sensors based on GHS effect have been studied by using a single chirped laser pulse [6]. It has also been shown that the sensitivity of bimetallic sensors based

* Authors to whom any correspondence should be addressed.



Original Content from this work may be used under the terms of the [Creative Commons Attribution 4.0 licence](https://creativecommons.org/licenses/by/4.0/). Any further distribution of this work must maintain attribution to the author(s) and the title of the work, journal citation and DOI.

on the graphene-hexagonal boron nitride heterostructure can be enhanced by increasing the GHS in the infrared band [7]. Likewise, giant GHS has been predicted theoretically [8–11] and demonstrated experimentally [12–15]. In a recent experiment, Sreekanth *et al* demonstrated a thirtyfold enhancement in GHS at the Brewster angle of a nanophotonic cavity operating at a given wavelength [12]. Zheng *et al* achieved a giant GHS by using magnetic dipole quasi-bound states in the continuum in dielectric metasurfaces [11]. Photonic heterostructures composed of two types of dielectric one-dimensional photonic crystals with symmetric unit cells can be used to significantly increase GHS, presenting a new promising method for design high-performance and sensitive sensors [9]. The GHS at the interface of topological materials, such as the topological edge states of a magnetic photonic crystal [16] and silicene [17] has also been recently investigated.

The GHS effect is not limited to light waves. Researchers have made significant advances using the GHS effect to solve many acoustic problems, which have aided our understanding of wave propagation. These advances have contributed to the development of new techniques to control and manipulate sound waves in different systems. For example, Zeng *et al* derived an analytic expression for the GHS occurring in acoustic metamaterial heterostructures [18], while FuPing *et al* and De Leo *et al* carried out the analysis on seismic waves [19, 20]. In addition, models of lateral displacement of acoustic wave scattering at a fluid-solid interface have revealed an acoustic analog of the GHS effect in optics [21]. Villegas *et al* investigated the relationship between tunneling of optical vibrational modes with transverse horizontal polarisation impinging on a semiconductor heterostructure together with the GHS [8]. Further research has revealed that the lateral shift of an optical beam undergoing Brillouin light scattering on an acoustic wave in the total internal reflection geometry depends on the polarization (longitudinal or transverse) of the acoustic wave [22]. Experimentally, acoustic GHS must be taken into account to design acoustic lenses, such as a flattened hemispherical acoustic Luneburg lens [23].

In this paper, we study the lateral shift experienced by both acoustic and optical vibrational modes upon reflection and transmission on both sides of a semiconductor layer sandwiched between two semi-infinite media. More specifically, we assess the impact of lateral shift of coupled longitudinal and transverse acoustic waves. These modes are excited by a longitudinal wave incident on the surface of a semiconductor layer at an oblique angle. To the best of our knowledge, this study is the first exploration of GHS in coupled vibrational modes. We compare the GHS with the length of the system and with the incident wavelength, and identify giant GHS in the structure.

We study the behaviour of the GHS in isotopically controlled ^{70}Ge layers. Over the past two decades, isotopically controlled semiconductors have garnered significant attention. These studies are particularly relevant because the nuclear mass difference directly impacts the phonon frequencies and related properties in crystalline solids, including lattice constant, thermal conductivity, electronic band gaps,

and localized vibrational modes [24]. For example, molecular dynamics simulations have shown that isotope mixing can effectively reduce the thermal conductivities of rectangular graphene nanoribbons [25]. Ultrafast studies of phonon transport in isotopically controlled semiconductor nanostructures have confirmed that isotopic modulation significantly decreases thermal conductivity beyond expectations in the coherent phonon transport regime [26]. Furthermore, Raman scattering measurements in germanium nanocrystals have exposed a rich multiple-peak structure, in addition to the well-known Ge–Ge peak at approximately 300 cm^{-1} of bulk Ge [27]. However, Raman spectroscopy analysis of $^{12}\text{C}/^{13}\text{C}$ graphene isotope superlattices demonstrates a different behaviour. While the Raman spectrum corresponds to the sum of the bulk ^{12}C and ^{13}C contributions for large periods, the formation of mixed $^{12}\text{C}/^{13}\text{C}$ modes is observed for Raman processes involving two phonons for small periods [28]. Moreover, *in situ* Raman spectroelectrochemistry has been adopted to study isotopically engineered graphene systems. This approach provides valuable information about the mutual interactions between graphene layers, their directly adjacent environment (e.g. substrate or electrolyte), and their extended environment separated by additional graphene layers [29]. Furthermore, the gradual introduction of heavier isotopes in the chemical vapor deposition growth of MoS_2 produces a systematic variation of the lattice phonon energy that modifies the transient and steady-state spontaneous photoluminescence spectra [30].

This work is organized as follows. Section 2 provides a concise overview of the general formalism utilized to describe the Goos–Hänchen effect. This includes an explanation of the stationary-phase approximation method, as well as the implementation of the long-wavelength continuum phenomenological model to describe vibrational modes in semiconductor heterostructures. The formalism established there will be used in section 3 to calculate the GHS for acoustic vibrational modes. In section 4, we focus on the analysis of the GHS for optical vibrational modes. We present numerical results for both longitudinal and transverse waves in a single-layer structure, demonstrating the validity of the analytical treatment presented in section 2. Finally, in section 5, we summarize the key findings of this study and draw our conclusions based on the obtained results.

2. Goos–Hänchen effect: general formalism

Figure 1 shows a schematic representation of the oblique incident problem addressed in this paper. The problem involves a semiconductor layer (spacer medium II) with thickness h sandwiched between two semi-infinite media, labelled as I and III, respectively. The thickness h is determined by the number of atomic layers comprising the spacer medium.

In our analysis, we assume a longitudinal (L) wave with an amplitude A_L^i incident at an angle θ_i onto the interface between media I and II, as depicted in figure 1. It is worth noting that for the elastic isotropic materials under investigation (Ge

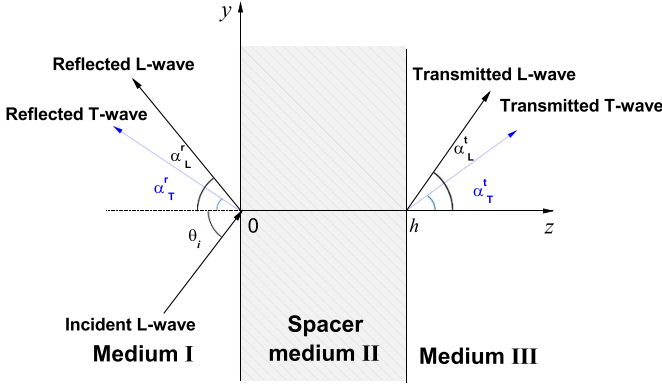


Figure 1. Schematic representation of the structure. The incident longitudinal L -wave forms an angle $\theta_i \equiv \alpha_L^i$ with the z -axis. Longitudinal (L) and transverse (T) waves are reflected in medium I forming angles α_L^r and α_T^r with the z -axis, respectively. Additionally, L and T waves are transmitted to medium III forming angles α_L^t and α_T^t with the z -axis, respectively.

isotopes), the propagation of oblique waves through the structure leads to non-degenerate transverse vibrational modes. Specifically, one of the transverse modes, polarized parallel to the interfaces and called shear mode (SH mode), remains decoupled from the other modes (transverse (SV) and longitudinal (L) modes). The SV and L modes are polarized in the sagittal plane (the plane defined by the wave vector and the unitary vector perpendicular to the interfaces), and are coupled to each other.

According to figure 1, at the interface $z=0$, the amplitudes of longitudinal and transverse reflected waves are A_L^r and A_T^r , respectively, with angles α_L^r and α_T^r . Additionally, at $z=h$, waves with amplitudes A_L^t and A_T^t , and angles α_L^t and α_T^t , respectively, are transmitted. The reflected and refracted angles are calculated using Snell's law. It is important to note that the wave propagation is confined into the yz -plane.

To investigate the Goos–Hänchen shift, we model the impinging displacement field, denoted by $\mathbf{u}_L^i(\mathbf{r}, t)$, as a two-dimensional wave packet propagating within the yz -plane. The incident wave packet can be written as [31],

$$\mathbf{u}_L^i(\mathbf{r}, t) = \int \frac{d^2k}{(2\pi)^2} \phi_L(\mathbf{k}) \mathbf{e}_L e^{i(\mathbf{k}\cdot\mathbf{r}-\omega t)}, \quad (1)$$

where $\mathbf{r} = (y, z)$ is the position vector, $\mathbf{k} = (k_y, k_z)$ is the wave vector, and \mathbf{e}_L is the polarization of the wave. We assume that the momentum distribution, denoted as $\phi_L(\mathbf{k})$, follows a Gaussian profile. The transmitted packet can be expressed as

$$\mathbf{u}_l^t(\mathbf{r}, t) = \int \frac{d^2k}{(2\pi)^2} \phi_l(\mathbf{k}) |t_l(\mathbf{k})| \mathbf{e}_l e^{i(\mathbf{k}\cdot\mathbf{r}-\omega t+\alpha_l^t)}, \quad (2)$$

where $t_l(\mathbf{k}) = |t_l(\mathbf{k})| e^{i\alpha_l^t}$ represents the amplitude of the transmitted wave, $l \in (L, T)$. The total phase of the transmitted mode can be written as,

$$\Psi_l^t = k_y y + k_z (z - h) - \omega t + \alpha_l^t. \quad (3)$$

If the width of the Gaussian energy distribution is sufficiently narrow, resembling a collimated beam, the transmission coefficients exhibit approximately constant magnitudes within the range of the integral. As result, the wave packet remains undistorted and does not undergo any reshaping [32]. When the stationary phase method is applied, the peak of the transmitted wave packet is located at the point where the phase of the transmitted wave packet becomes stationary. Therefore, both the partial derivatives of Ψ_l^t in equation (3) with respect to the incident angle (θ_i) and with respect to the frequency (ω) must vanish,

$$\left. \frac{\partial \Psi_l^t}{\partial \theta_i} \right|_{\omega} = 0, \quad (4)$$

$$\left. \frac{\partial \Psi_l^t}{\partial \omega} \right|_{\theta_i} = 0. \quad (5)$$

Let us assume that the peak of the transmitted packet within medium III is located at $\mathbf{r} = (\Delta y_l^t, h)$. By substituting equation (3) into equations (4) and (5), we obtain the following expression for the GHS of the transmitted packet,

$$\Delta y_l^t = - \left(\frac{\partial k_y}{\partial \theta_i} \right)^{-1} \frac{\partial \alpha_l^t}{\partial \theta_i}. \quad (6)$$

Similarly, the reflected wave packet \mathbf{u}_l^r can be expressed as

$$\mathbf{u}_l^r(\mathbf{r}, t) = \int \frac{d^2k}{(2\pi)^2} \phi_l(\mathbf{k}) |r_l(\mathbf{k})| \mathbf{e}_l e^{i(k_y y - k_z z - \omega t + \alpha_l^r)}, \quad (7)$$

where $r_l(\mathbf{k}) = |r_l(\mathbf{k})| e^{i\alpha_l^r}$ represents the amplitude of the reflected wave. The corresponding total phase of the reflected modes is given by

$$\Psi_l^r = k_y y - k_z z - \omega t + \alpha_l^r. \quad (8)$$

We assume that the peak of the reflected packet within medium I is located at $\mathbf{r} = (\Delta y_l^r, 0)$. Similarly to the previous case, the GHS for the reflected packet can be written as

$$\Delta y_l^r = - \left(\frac{\partial k_y}{\partial \theta_i} \right)^{-1} \frac{\partial \alpha_l^r}{\partial \theta_i}. \quad (9)$$

In this work, acoustic and optical vibrations in semiconductor material are described within the framework of the long-wavelength continuum phenomenological model [33, 34]. This model provides a suitable description for nanostructures such as those studied here, whose dimensions are in the order of a few atomic layers [35]. Within this model, the propagation of acoustic and optical waves can be described by the following equation of motion

$$\rho \frac{\partial^2 \mathbf{u}}{\partial t^2} = -\rho \omega_\Gamma^2 \mathbf{u} + \nabla \cdot \boldsymbol{\sigma}. \quad (10)$$

Here, \mathbf{u} represents the displacement field, ρ is the mass density, ω_Γ is the phonon frequency at the center of the Brillouin zone,

and σ is the stress tensor. The components of the stress tensor can be expressed as

$$\sigma_{ij} = -\rho(\beta_L^2 - 2\beta_T^2)(\nabla \cdot \mathbf{u})\delta_{ij} - \rho\beta_T^2(\nabla_i u_j + \nabla_j u_i), \quad (11)$$

where β_L and β_T are two parameters that describe the dispersion relations of the longitudinal and transverse oscillations. For optical branches, the dispersion relation in the neighbourhood of the Γ point of the Brillouin zone is given by the parabolic function $\omega^2(\mathbf{k}) = \omega_l^2 - \beta_l^2 k_l^2$. For acoustic branches, the dispersion relation is a linear function of the form $\omega(\mathbf{k}) = v_l k_l$, where v_l represents the sound velocity.

The reflection coefficient ($\mathcal{R}_l = j_l^r/j_l^i$) and transmission coefficient ($\mathcal{T}_l = j_l^t/j_l^i$) can be defined as the ratios of the reflected and transmitted fluxes to the incident flux, respectively [34]. The reflected flux is given by $j_l^r = \rho\omega k_l(k_y^2 + k_z^2)\beta_l^2 |A_l^r|^2$, and the transmitted flux is given by $j_l^t = \rho\omega k_l(k_y^2 + k_z^2)\beta_l^2 |A_l^t|^2$. To calculate j_l^r and j_l^t , the parameters corresponding to media I and III must be considered. The incident flux is given by $j_l^i = \rho\omega k_l(k_y^2 + k_z^2)\beta_l^2 |A_l^i|^2$, where $A_l^i = 1$. A_l^r and A_l^t are calculated using the transfer matrix method.

3. Goos–Hänchen shift for acoustic vibrational modes

In this section, we apply the previously presented formalism to calculate the GHS for the system described earlier. The longitudinal P-waves and transverse SV-waves, which are polarized in the yz -plane, are coupled at the interfaces between different layers in the system. However, SH-waves, with polarization normal to the yz -plane, do not interact with the P- and SV-waves and can be considered separately. Here, we focus on coupled P-SV waves and exclude SH-waves, which has been studied in a previous work [8].

Let us assume that a longitudinal wave with an amplitude $u_i = A_L^i e^{i(k_y y + k_z z)}$ is incident on the interface between media I and II, where $k_y = k_i \sin(\theta_i)$, $k_z = k_i \cos(\theta_i)$, and $k_i = \frac{\omega}{v_{L1}}$. The total scattered field is a combination of leftward- and rightward-propagating waves, including both propagating and evanescent modes. The wavenumber of an evanescent mode is purely imaginary. Furthermore, the wave vector components along the interface are conserved.

The components of the displacement field in regions I, II, and III are solutions of equation (10) satisfying the boundary conditions at the interface, i.e. the continuity of the displacement field and the stress tensor [35]. For simplicity, we assume identical media for regions I and III. Under this simplification, the z component of the wave vectors in regions I and III can be written as $k_{L1} = k_{L3} = \frac{\omega}{v_{L1}} \cos(\theta_i)$ and $k_{T1} = k_{T3} = \frac{\omega}{v_{T1}} \sqrt{1 - \frac{v_{T1}^2}{v_{L1}^2} \sin^2(\theta_i)}$. If the incidence angle in medium I is equal to

$$\theta_{c1} = \arcsin(v_{L1}/v_{L2}), \quad (12)$$

the refracted angle in medium II becomes $\alpha_{L2} = \frac{\pi}{2}$. For $\theta_i > \theta_{c1}$, $k_{L2} = \frac{\omega}{v_{L2}} \sqrt{1 - \frac{v_{L2}^2}{v_{L1}^2} \sin^2(\theta_i)}$ becomes purely imaginary, and the corresponding longitudinal mode in medium II is evanescent. The second critical angle θ_{c2} occurs when the refracted transverse angle becomes $\alpha_{T2} = \frac{\pi}{2}$. Consequently,

$$\theta_{c2} = \arcsin(v_{L1}/v_{T2}), \quad (13)$$

hence, $k_{T2} = \frac{\omega}{v_{T2}} \sqrt{1 - \frac{v_{T2}^2}{v_{L1}^2} \sin^2(\theta_i)}$ is imaginary and its corresponding transverse mode is evanescent. Moreover, we can derive an additional angle from the condition $k_{T1} = 0$, which can be written as

$$\theta_{c3} = \arcsin(v_{L1}/v_{T1}). \quad (14)$$

This condition indicates that, when $\theta_i > \theta_{c3}$, both the reflected and transmitted transverse modes are evanescent.

Numerical simulations were performed for media I and III consisting of ^{74}Ge , and a spacer layer II composed of four atomic layers of ^{70}Ge with thickness $h = 5.7 \text{ \AA}$.

The velocities of the longitudinal and transverse acoustic waves, normalized to the speed of light, travelling through ^{74}Ge are $v_{L1} = 2.35 \times 10^{-6}$ and $v_{T1} = 1.32 \times 10^{-6}$, respectively. Similarly, in ^{70}Ge , the normalized velocities are $v_{L2} = 2.41 \times 10^{-6}$ and $v_{T2} = 1.36 \times 10^{-6}$ for longitudinal and transverse waves, respectively. Because both materials exhibit linear dispersion relations for acoustic modes, the frequency in the center of the Brillouin zone is zero, $\omega_L = \omega_T = 0$.

The approximate value for the first critical angle between ^{74}Ge and ^{70}Ge is $\theta_{c1} \approx 76.76^\circ$. However, when attempting to calculate the second critical angle, θ_{c2} , between the two materials, it is found that such an angle does not exist because $\sin(\theta_{c2}) > 1$. This means that refracted angles are smaller than incident angles when the wave velocity in the second material is slower than in the first material. On the other hand, refracted angles are larger than incident angles when the wave velocities in the second material are greater than in the first material. Since $v_{L1} > v_{T1}$, the third critical angle θ_{c3} is complex.

The expressions for the Goos–Hänchen shift for transmitted (equation (6)) and reflected waves (equation (9)) can be simplified to the following expressions by considering the linear dispersion relation for acoustic vibrational modes,

$$\Delta y_L^t = -\frac{v_{L3}}{\omega \cos(\theta_i)} \frac{\partial \alpha_L^t}{\partial \theta_i}, \quad (15)$$

$$\Delta y_L^r = -\frac{v_{L1}}{\omega \cos(\theta_i)} \frac{\partial \alpha_L^r}{\partial \theta_i}. \quad (16)$$

It is worth stressing that when the angle of incidence is equal to the critical angle θ_{c1} , total internal reflection of the longitudinal mode occurs. Therefore, the amplitude of the wave in region II (see figure 1) decays exponentially in the z direction and propagates in the y direction up to a distance Δy_L^r (GHS in reflection). The energy tunneled through medium II emerges at the point $(h, \Delta y_L^r)$ as a longitudinal wave transmitted in medium III, where Δy_L^t is the GHS in reflection.

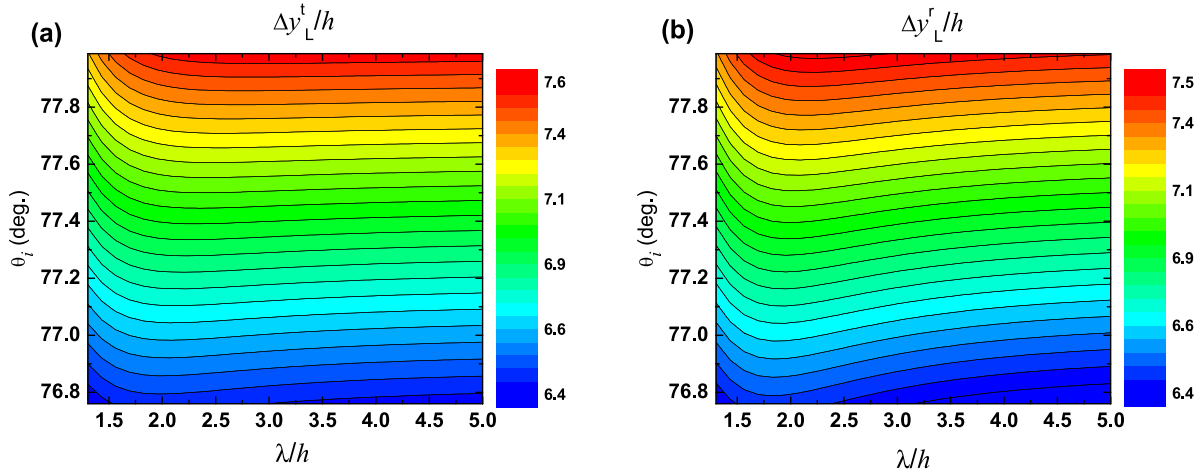


Figure 2. GHS generated by the structure illustrated in figure 1 as a function of the wavelength (λ) and the incidence angle (θ_i) for (a) transmitted (Δy_L^t) and (b) reflected (Δy_L^r) longitudinal waves. Δy_L^t , Δy_L^r , and λ are normalized to the layer thickness h .

Figure 2 shows the GHS calculated from equations (15) and (16) as a function of wavelength (λ) and incidence angle (θ_i), for θ_i greater than the first critical angle $\theta_{c_1} \approx 76.76^\circ$. Figure 2(a) represents the GHS for transmitted acoustic waves (Δy_L^t), while figure 2(b) depicts the GHS for reflected acoustic modes (Δy_L^r). Both Δy_L^t and Δy_L^r are normalized to the layer thickness h . It is observed that both Δy_L^t and Δy_L^r increase when we increase the incident angle. The contour map of figure 2 exhibit a non-monotonic behaviour, as a function of λ , which is more pronounced in the case of Δy_L^r . From equations (15) and (16), it is inferred that the GHS is proportional to the phase variation with respect to the angle of incidence θ_i and inversely proportional to $\cos(\theta_i)$. Due to the weak dependence of the transmitted and reflected phases on θ_i , an increase of θ_i implies an increase of the GHS observed for Δy_L^t and Δy_L^r in figures 2(a) and (b), respectively. Remarkably, the GHS is found to be more than six times larger than the structural thickness and even exceeds the wavelength within the spectral window depicted in figure 2.

Figure 3 displays selected cuts from the contour plots of figure 2 at specific incident angles: (a) $\theta_i = 76.76^\circ$, (b) $\theta_i = 78^\circ$, (c) $\theta_i = 80.0^\circ$, and (d) $\theta_i = 84.0^\circ$. In particular, figure 3(a) presents the GHS at the first critical angle, $\theta_i = \theta_{c_1}$. It can be observed that both the transmitted (black line) and reflected (red line) acoustic modes exhibit a similar trend, characterized by a maximum value of the GHS. A similar behaviour is observed in figure 3(b) for a slightly larger angle $\theta_i = 78^\circ$. However, if the incident angle increases further, such as $\theta_i = 80^\circ$ and $\theta_i = 84^\circ$ (see figures 3(c) and (d)), the peak disappears, and the GHS increases monotonically with respect to λ until it reaches a saturation value. It is noteworthy that as θ_i becomes larger, the transmitted GHS (Δy_L^t) becomes similar to the reflected GHS (Δy_L^r). In fact, both curves are practically indistinguishable at $\theta_i = 84^\circ$. Note that, as expected, the GHS varies significantly when the wavelength is of the order of the scattering material's thickness, while it remains practically constant for $\lambda \gg h$. This is because the incident wave is unable to resolve the inhomogeneities it encounters in the transmitting medium.

The differences observed between Δy_L^t and Δy_L^r are attributed to the coupling with transverse modes. Figures 3(a)–(c) show that Δy_L^t and Δy_L^r intersect at a value of λ , denoted as λ_c . The following values are obtained: $\lambda_c/h = 2.58$ and $\Delta y_L/h = 6.44$ for $\theta_i = 76.76^\circ$; $\lambda_c/h = 2.60$ and $\Delta y_L/h = 7.57$ for $\theta_i = 78.0^\circ$; and $\lambda_c/h = 2.62$ and $\Delta y_L/h = 10.38$ for $\theta_i = 80.0^\circ$. It is worth noting that λ_c increases as θ_i increases. Furthermore, for these angles, near the first critical angle, $\Delta y_L^t > \Delta y_L^r$ when $\lambda < \lambda_c$, while $\Delta y_L^t < \Delta y_L^r$ when $\lambda > \lambda_c$. However, for larger angles, as is shown in figure 3(d), $\Delta y_L^t \cong \Delta y_L^r$ for all values of λ , as mentioned before. Although for simpler systems it is possible to provide a rigorous analytical demonstration of the equality of tunneling times for transmitted and reflected wave packets [36, 37], the numerical verification that the phase difference equals the constant term $\pi/2$ allows us to ensure that this property also holds, under the conditions analyzed here, when considering coupled longitudinal and transverse modes.

So far, we have compared the GHS with the layer thickness. However, it is also valuable to consider its comparison with the wavelength. Figure 4 presents the transmitted GHS normalized to λ . It can be observed that $\Delta y_L^t/\lambda$ increases when we increase the incident angle and decrease the wavelength, and that a GHS is obtained almost 20 times larger than the wavelength.

The GHS as a function of the transmission (t_L) and reflection (r_L) amplitudes from equations (6) and (9) can be written as,

$$\Delta y_L^t = - \frac{(\Re(t_L) \partial_{\theta_i} \Im(t_L) - \Im(t_L) \partial_{\theta_i} \Re(t_L))}{\mathcal{T}_L} \left(\frac{\partial k_y}{\partial \theta_i} \right)^{-1}, \quad (17)$$

$$\Delta y_L^r = - \frac{(\Re(r_L) \partial_{\theta_i} \Im(r_L) - \Im(r_L) \partial_{\theta_i} \Re(r_L))}{\mathcal{R}_L} \left(\frac{\partial k_y}{\partial \theta_i} \right)^{-1} \quad (18)$$

where \Re and \Im denote real part and imaginary part, respectively. It can be seen, from equations (17) and (18), that the behaviour of the GHS is influenced by the transmission and reflection coefficients. Figure 5 displays the reflection and

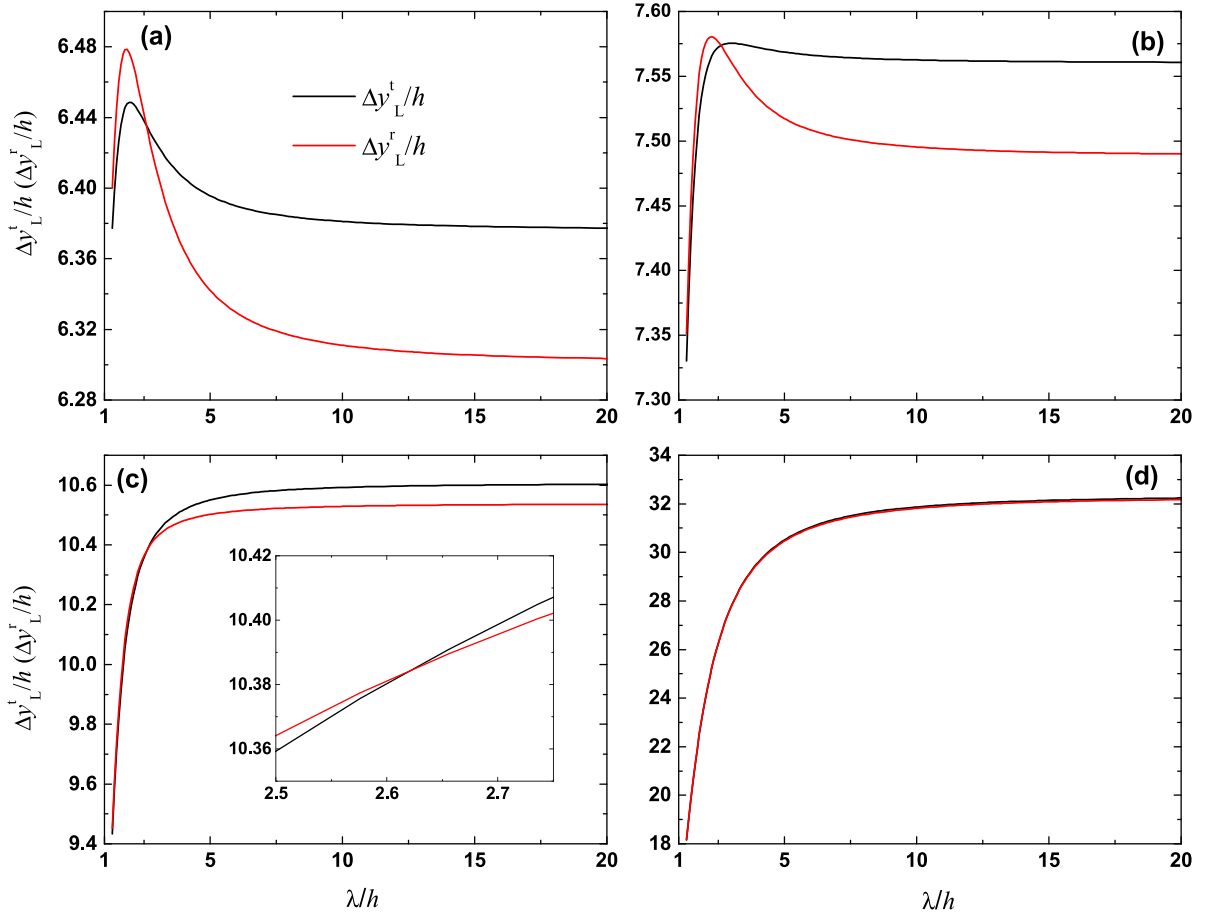


Figure 3. Transmitted (Δy_L^t) and reflected (Δy_L^r) longitudinal GHS as a function of wavelength (λ) for incident angles (a) $\theta_i = 76.76^\circ$, (b) $\theta_i = 78^\circ$, (c) $\theta_i = 80.0^\circ$, and (d) $\theta_i = 84.0^\circ$. Δy_L^t , Δy_L^r , and λ are normalized to the layer thickness h . The inset in (c) is a zoom of the intersection between Δy_L^t and Δy_L^r .

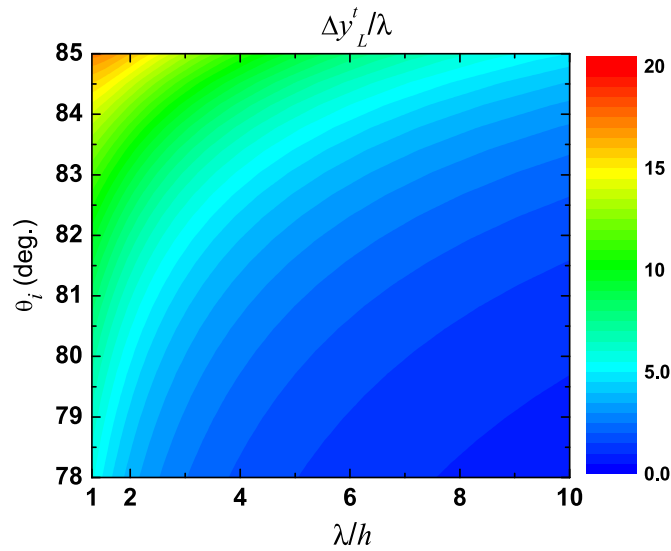


Figure 4. Normalized GHS $\Delta y_L^t/\lambda$ as a function of λ/h and θ_i .

transmission coefficients \mathcal{R}_L , \mathcal{R}_T , \mathcal{T}_L , and \mathcal{T}_T as a function of λ and θ_i . These coefficients satisfy the identity $\mathcal{T}_L + \mathcal{R}_L + \mathcal{T}_T + \mathcal{R}_T = 1$, if, as in this work, absorption is not considered. In the post-critical region where $\theta_i > \theta_{c1}$, longitudinal modes

become evanescent. Consequently, \mathcal{T}_L grows as θ_i decreases and λ increases, approaching rapidly to the case of perfect transmission ($\mathcal{T}_L = 1$) as shown in figure 5(a). However, Δy_L^t increases when we increase the angle of incidence and

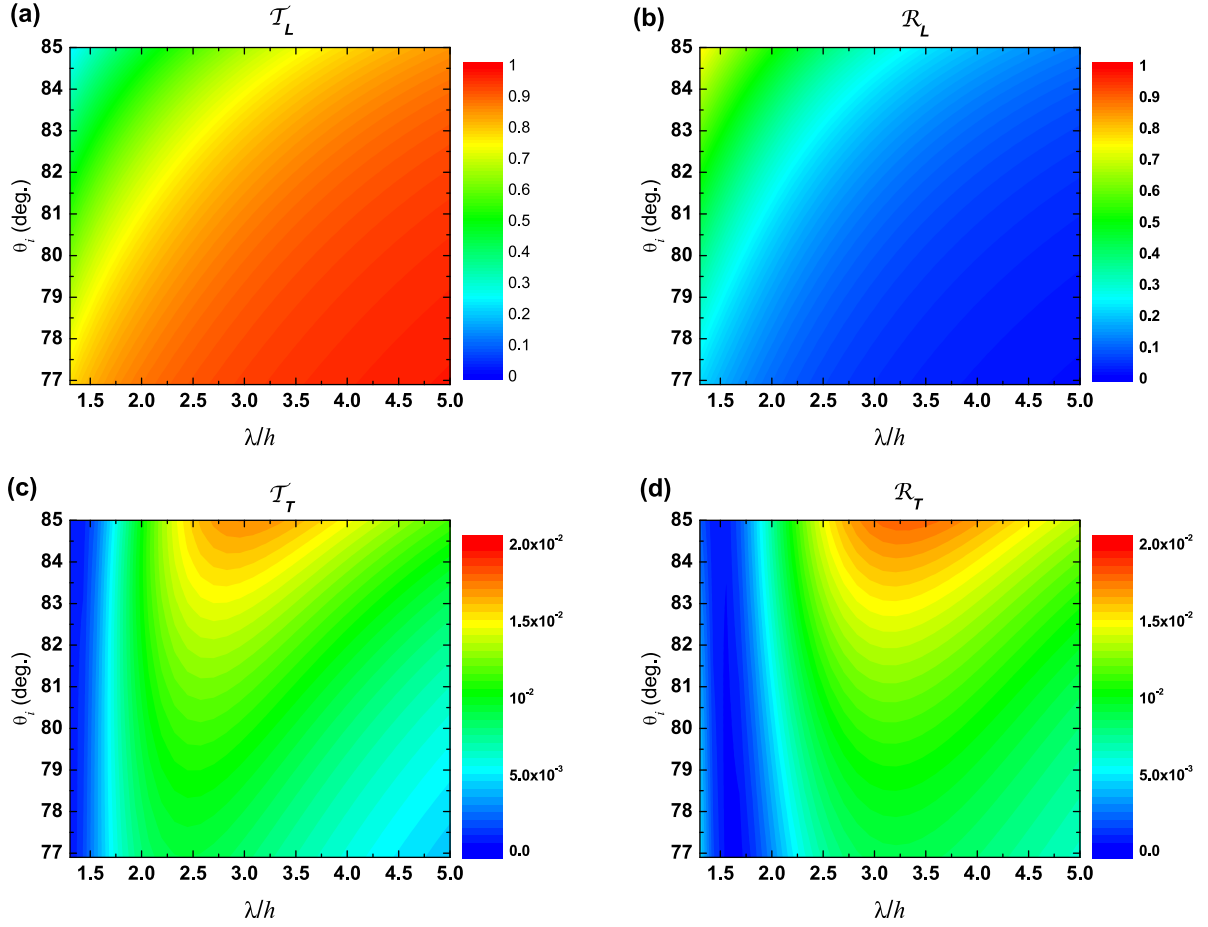


Figure 5. Transmission and reflection coefficients for longitudinal and transverse acoustic modes as a function of the normalized wavelength λ/h and the incidence angle θ_i .

decrease the wavelength. Since the coefficients \mathcal{T}_T and \mathcal{R}_T for transverse modes are very small (see figures 5(c) and (d)), we have $\mathcal{R}_L \approx 1 - \mathcal{T}_L$. Despite the relatively small values of \mathcal{T}_T and \mathcal{R}_T , the coupling between longitudinal (L) and transverse (T) modes leads to the observed differences between the transmitted and reflected GHS depicted in figures 2 and 3. This coupling effect plays a crucial role in the behaviour of the GHS and contributes to the distinctive features observed in the plots.

4. Goos–Hänchen shift for optical vibrational modes

In this section, we study the GHS for optical vibrations. Similar to the previous section, we examine the case of an optical longitudinal wave incident on a ^{70}Ge layer sandwiched between two isotropic half-spaces of ^{74}Ge (see figure 1). At the Γ point of the Brillouin zone, the ^{74}Ge and ^{70}Ge atoms exhibit a frequency value of approximately $\omega_{T_1} = \omega_{L_1} \approx 301.5 \text{ cm}^{-1}$ and $\omega_{T_2} = \omega_{L_2} \approx 309.4 \text{ cm}^{-1}$, respectively. The parameters $\beta_{L_1}^2 = 2.8 \times 10^{-12}$ and $\beta_{T_1}^2 = 4 \times 10^{-12}$, normalized to the speed of light, are employed for both isotopes, as reported in [34].

In this case, the relevant components of the wavevector in media I and III can be expressed as follows:

$$k_y = \sin(\theta_i) \sqrt{\frac{\omega_{L_1}^2 - \omega^2}{\beta_{L_1}^2}},$$

$$k_{L_1} = k_{L_3} = \cos(\theta_i) \sqrt{\frac{\omega_{L_1}^2 - \omega^2}{\beta_{L_1}^2}},$$

$$k_{T_1} = k_{T_3} = \sqrt{\left(\frac{\omega_{T_1}^2 - \omega^2}{\beta_{T_1}^2}\right) \left(1 - \frac{\beta_{T_1}^2}{\beta_{L_1}^2} \sin^2(\theta_i)\right)}.$$

According to the procedure described in section 3, the critical angles can be obtained as a function of the frequency. In particular, from the Snell's law, we obtain two critical angles. The first critical angle, denoted as θ_{c_1} , is defined as

$$\theta_{c_1} = \arcsin\left(\frac{\beta_{L_1}}{\beta_{L_2}} \sqrt{\frac{\omega_{L_2}^2 - \omega^2}{\omega_{L_1}^2 - \omega^2}}\right). \quad (19)$$

Therefore, for $\theta_i > \theta_{c_1}$, the longitudinal mode becomes evanescent because

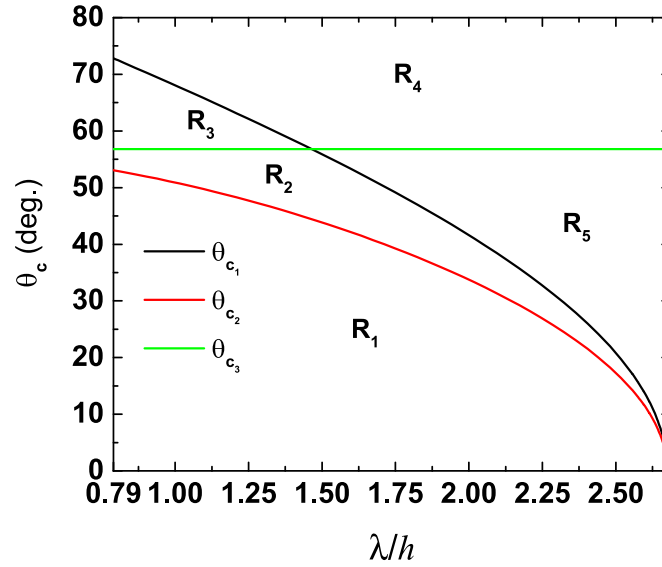


Figure 6. Critical angles θ_{c_1} (black line), θ_{c_2} (red line) and θ_{c_3} (green line) versus the normalized wavelength λ/h .

$$k_{L_2} = \sqrt{\left(\frac{\omega_{L_2}^2 - \omega^2}{\beta_{L_2}^2}\right) \left(1 - \frac{\beta_{L_2}^2 (\omega_{L_1}^2 - \omega^2)}{\beta_{L_1}^2 (\omega_{L_2}^2 - \omega^2)} \sin^2(\theta_i)\right)},$$

is imaginary. The second critical angle, denoted as θ_{c_2} , is given by

$$\theta_{c_2} = \arcsin\left(\frac{\beta_{L_1}}{\beta_{T_2}} \sqrt{\frac{\omega_{T_2}^2 - \omega^2}{\omega_{L_1}^2 - \omega^2}}\right). \quad (20)$$

For $\theta_i > \theta_{c_2}$, the transverse mode becomes evanescent because,

$$k_{T_2} = \sqrt{\left(\frac{\omega_{T_2}^2 - \omega^2}{\beta_{T_2}^2}\right) \left(1 - \frac{\beta_{T_2}^2 (\omega_{L_1}^2 - \omega^2)}{\beta_{L_1}^2 (\omega_{T_2}^2 - \omega^2)} \sin^2(\theta_i)\right)},$$

is also imaginary. Additionally, it should be noted that k_{T_1} has only real values for incident angles less than the critical angle θ_{c_3} , given by

$$\theta_{c_3} = \arcsin\left(\frac{\beta_{L_1}}{\beta_{T_1}}\right). \quad (21)$$

For incident angles greater than θ_{c_3} , k_{T_1} becomes imaginary, indicating the presence of an evanescent wave.

In figure 6, the critical angles θ_{c_1} (black line), θ_{c_2} (red line), and θ_{c_3} (green line) are shown as a function of the wavelength in the spectral window from $\lambda/h = 0.79$ to $\lambda/h = 2.67$. It is worth noting that λ can be computed in terms of the frequency using the relation $\lambda = 2\pi\beta_{L_1}/\sqrt{\omega_{L_1}^2 - \omega^2}$. In this figure, the $\theta_i - \lambda/h$ -plane is divided in five different regions. Region \mathbf{R}_1 corresponds to all the values of λ/h and θ_i below θ_{c_2} . In

this region the wavenumbers are real, and both longitudinal and transverse modes propagate in the structure. In region \mathbf{R}_2 , defined by the intersection of the different critical angles the wavenumber k_{T_2} becomes imaginary, indicating that the transverse mode is evanescent within the layer. k_{T_1} and k_{T_2} are both imaginary in \mathbf{R}_3 . Therefore, the transverse modes are evanescent within and outside the layer, while the longitudinal modes are propagating. In region \mathbf{R}_4 , k_{L_2} , k_{T_2} , and k_{T_1} are imaginary, indicating that the transverse and the longitudinal modes are nonpropagating within and outside the layer. Finally, in region \mathbf{R}_5 , k_{L_2} and k_{T_2} are imaginary and only evanescent modes are present within the layer.

Because the GHS is observed for evanescent modes, the optical transverse modes experience GHS in regions \mathbf{R}_2 , \mathbf{R}_3 , \mathbf{R}_4 , and \mathbf{R}_5 . Meanwhile, the optical longitudinal modes experience GHS in regions \mathbf{R}_4 and \mathbf{R}_5 only. Figures 7 and 8 illustrate the GHS for the L and T optical modes, respectively.

In figure 7(a), we present the plot of $\Delta y_L^t/h$ as a function of the wavelength for five different incident angles in the region \mathbf{R}_4 . We observe that Δy_L^t exhibits values approximately one order of magnitude larger than h when λ is approximately $0.8h$. Furthermore, larger values of Δy_L^t are obtained as the incidence angle θ_i increases. However, Δy_L^t gradually decreases if the wavelength increases. It should be noted that the most substantial enhancements of Δy_L^t occur when the wavelength λ is close to the thickness of the layer h . Consequently, the enhancement of Δy_L^t with respect to λ is comparable to the enhancement with respect to h . For completeness, we also present in figure 7(b) the plot of $\Delta y_L^t/\lambda$. We find a remarkable giant GHS, as large as 30 times the value of λ for the smallest wavelengths and largest incidence angles.

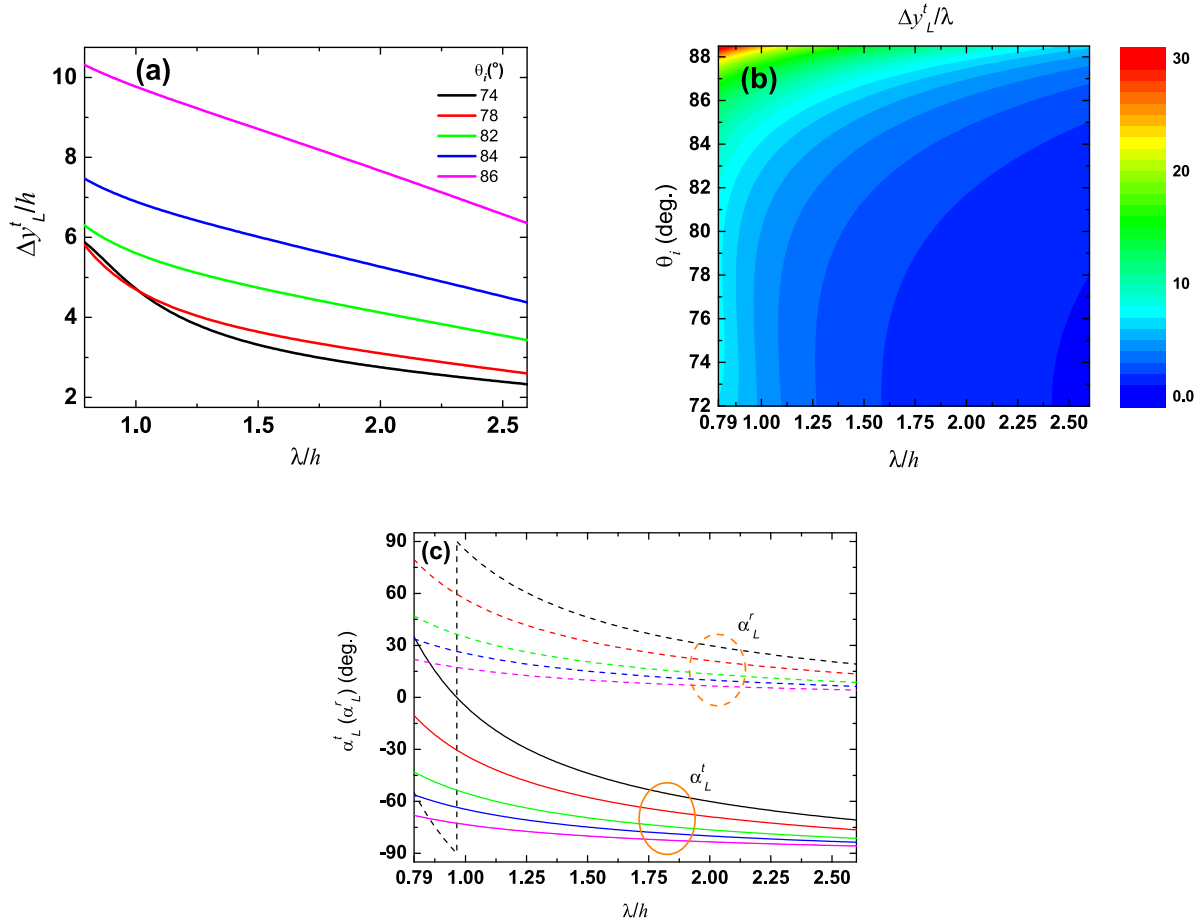


Figure 7. (a) Normalized GHS as a function of the normalized wavelength λ/h for transmitted longitudinal mode, at $\theta_i = 74^\circ$ (black line), $\theta_i = 78^\circ$ (red line), $\theta_i = 82^\circ$ (green line), $\theta_i = 84^\circ$ (blue line), and $\theta_i = 86^\circ$ (magenta line). (b) Contour map of the normalized GHS versus λ/h and θ_i . (c) Transmitted (solid lines) and reflected (dashed lines) phases for the angles considered in (a).

An intriguing and noteworthy aspect of the GHS is that the transmitted and reflected GHS are equal for longitudinal modes in region \mathbf{R}_4 . The physical character of this result is associated with the behaviour of the reflected (α_L^r) and transmitted (α_L^t) phases, displayed in figure 7(c). Through a numerical calculation (not shown here), it has been determined that the phase difference $\Delta\alpha(\lambda, \theta_i) = \alpha_L^t - \alpha_L^r$ is approximately $\pm\pi/2$. Consequently, α_L^t and α_L^r have almost the same slope ($\partial\alpha_L^t/\partial\theta_i \approx \partial\alpha_L^r/\partial\theta_i$). If these slope values are substituted into equations (6) and (9), we find that $\Delta y_L^t \approx \Delta y_L^r$. In summary, the behaviour of the phase difference between the transmitted and reflected longitudinal optical modes, shown in figure 7(c), allows us to ensure that there are regions within the plane $(\theta_i, \lambda/h)$ where, jointly, the general principles of temporal reversal invariance, spatial reversal invariance, and conservation of energy density flux are satisfied, similar to the one-dimensional and two-dimensional problems described above.

Figure 8 illustrates the GHS for transverse modes at some representative angles within regions from \mathbf{R}_2 to \mathbf{R}_5 , as described in figure 6. The upper panel focuses on the

region \mathbf{R}_4 , while the middle panel depicts curves starting in the region \mathbf{R}_3 and entering \mathbf{R}_4 as λ increases (see figure 6). Similarly, the lower panel includes regions \mathbf{R}_2 and \mathbf{R}_5 . In the left panels, the GHS is normalized to λ , while in the right panels the corresponding GHS curves are normalized to h .

In contrast to the behaviour observed for longitudinal modes in figure 7, the GHS exhibits distinct characteristics for transmitted and reflected transverse modes in region \mathbf{R}_4 . Specifically, we observe that the GHS for transmitted modes (Δy_T^t) is larger than the GHS for reflected modes (Δy_T^r). Within region \mathbf{R}_4 , both Δy_T^t and Δy_T^r show a monotonically decaying trend, as depicted in figure 8(a). From figure 8(d) it can be seen that the GHS for transmitted modes normalized to h decreases until certain value of λ/h and then grows slightly, this growth being more pronounced for the angle of 85° . On the other hand, $\Delta y_T^r/h$ and $\Delta y_T^r/\lambda$, depicted in dashed lines in figures 8(a) and (d), show a similar behaviour. Moreover, within this region, as the angle of incidence increases the GHS for reflected and transmitted transverse modes also increases.

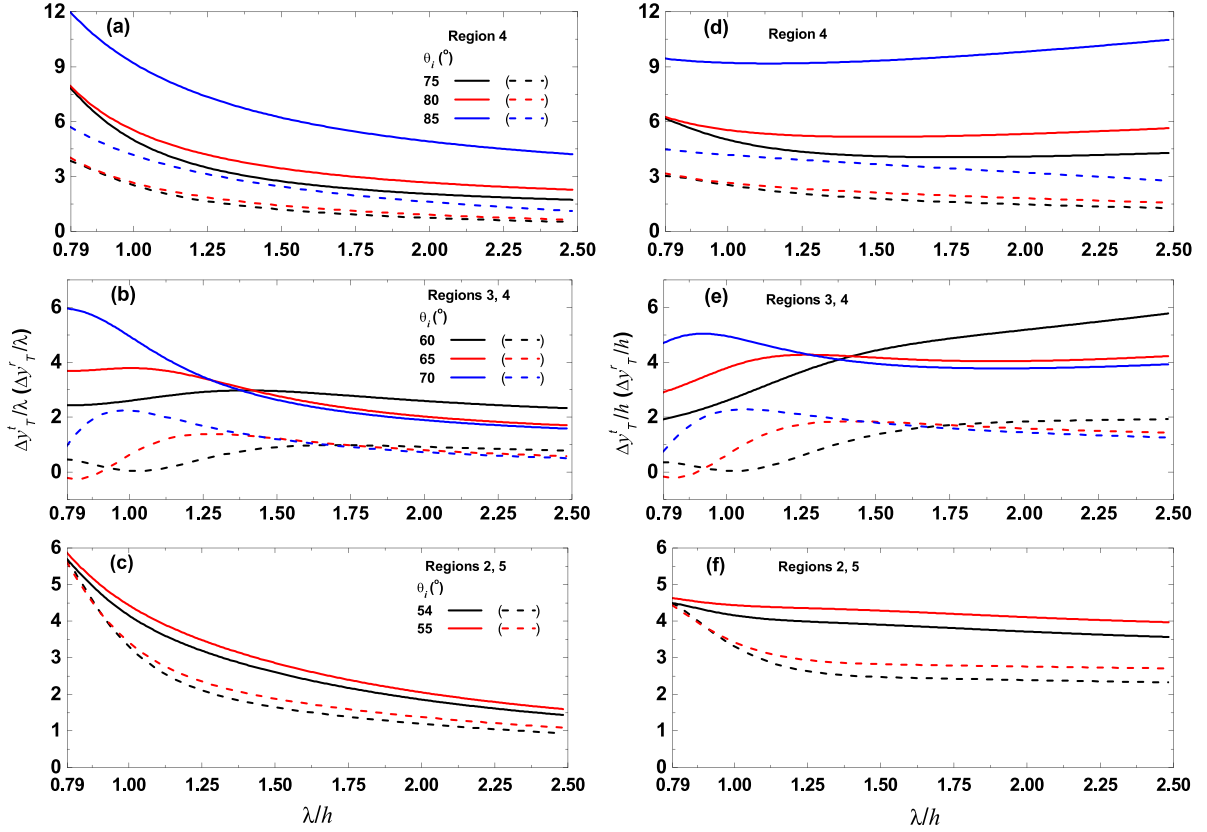


Figure 8. GHS is shown as a function of λ for transmitted (solid lines) and reflected (dashed lines) transverse modes at various angles in regions (a) \mathbf{R}_4 , (b) \mathbf{R}_3 , \mathbf{R}_4 , and (c) \mathbf{R}_2 , \mathbf{R}_5 . GHS is normalized to λ , while lambda in the horizontal axis is normalized to h . Panels (d), (e), and (f) display the h -normalized GHS of (a), (b), and (c) respectively.

However, in regions \mathbf{R}_3 and \mathbf{R}_4 , these quantities exhibit non-monotonic behaviour as functions of both λ and θ_i , as shown in figures 8(b) and (e). These unusual trends arise due to the coupling of L and T modes. Although T modes are evanescent in both regions \mathbf{R}_3 and \mathbf{R}_4 , they are coupled with L modes, which propagate in \mathbf{R}_3 and decay in region \mathbf{R}_4 . The trends in the curves change at the boundary between these two regions, where λ/h is between 1.25 and 1.50. On the left side of this boundary, in region \mathbf{R}_3 , the GHS increases with θ_i . Conversely, in region \mathbf{R}_4 , on the right side of the boundary, the GHS shows the opposite behaviour. Notably, for the smallest values of the wavelength ($0.79 < \lambda/h < 0.90$) and an incidence angle of $\theta_i = 65^\circ$, the GHS of the reflected waves takes negative values, indicating an intriguing behaviour in this specific regime. Since phase changes depend on the interaction between the modes, they can be positive or negative. These phase changes are associated with the existence of GHS of both signs. For example, in a hybrid surface plasmon resonance sensor structure based on Cu-BlueP/TMDC-graphene, Z-shaped to Lorentzian-like phase changes produce GHS shifts from positive to negative [38]. For our system, a numerical study of the behaviour of the phase associated with the reflected transverse mode, in the region considered above, shows an ascending

convex curve and as a consequence the corresponding GHS is negative.

Finally, in regions \mathbf{R}_2 and \mathbf{R}_5 , analyzed in figures 8(c) and (f), the GHS exhibits similar trends to those observed in region \mathbf{R}_4 .

For completeness, figure 9 presents the reflection and transmission coefficients for optical modes at oblique incidence. These coefficients provide insight into the energy conversion in different scattering channels. In particular, the coefficients exhibit an abrupt change in slope at the critical angle ($\theta_{c_3} = 56.79^\circ$). For high incident angles in region \mathbf{R}_4 ($\theta_i > 73^\circ$), the longitudinal mode becomes evanescent. Consequently, almost all of the energy is reflected ($\mathcal{R}_L \approx 1$, see figure 9(b)). However, the evanescent longitudinal wave is still capable of excite longitudinal vibrations in the region $z > h$, resulting in nonzero transmission ($\mathcal{T}_L \neq 0$, see figure 9(a)). Furthermore, it can be observed that in the interval $60^\circ < \theta_i < 70^\circ$, for regions \mathbf{R}_3 and \mathbf{R}_4 , the coefficient \mathcal{R}_T consistently exceeds the coefficient \mathcal{T}_T (see figures 9(c) and (d)) regardless of the incident angle and the frequency. In this interval, the transverse mode is evanescent. As a result, the frustrated total internal reflection typically exhibits a larger $\Delta y_T^t/h$ compared to $\Delta y_T^t/h$.

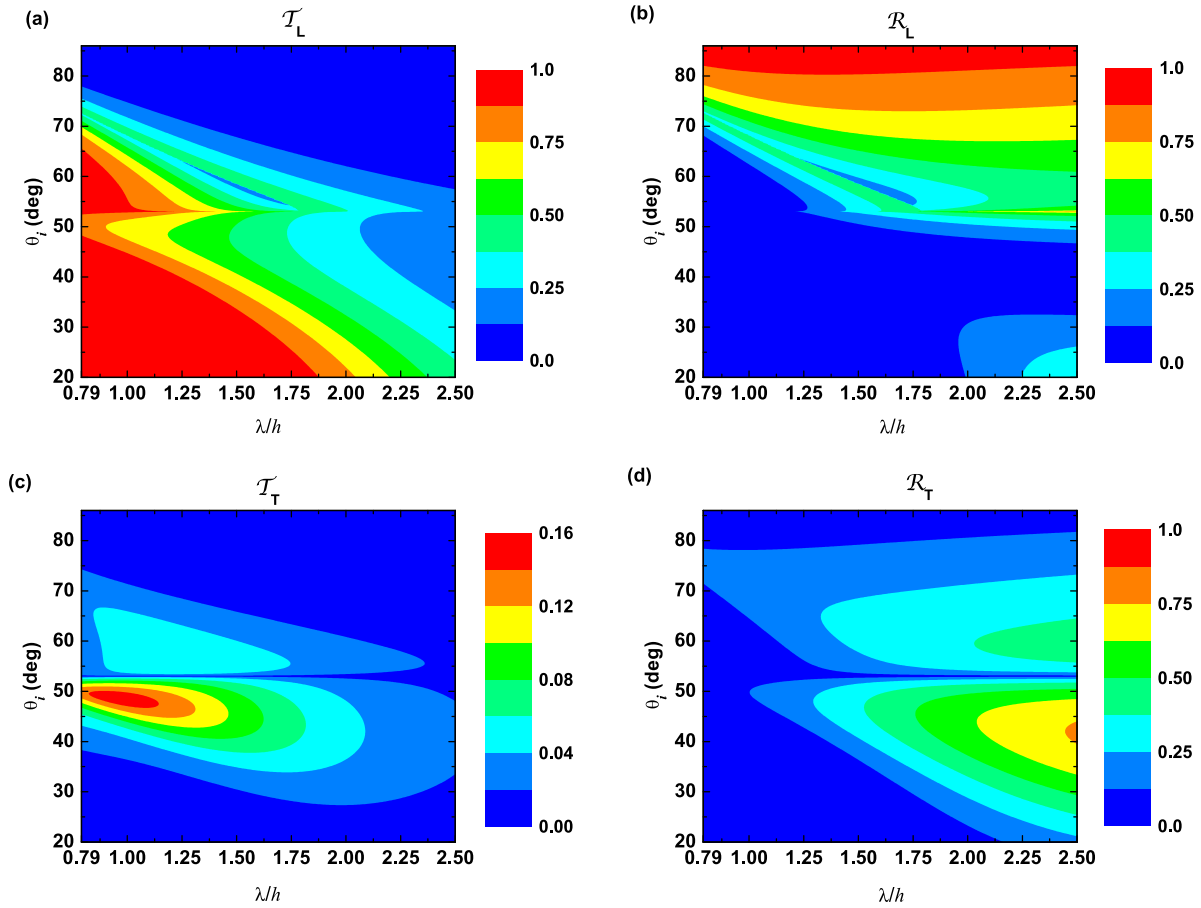


Figure 9. The transmission and reflection coefficients, \mathcal{T} and \mathcal{R} , respectively as a function of the incident angle and the normalized wavelength for both longitudinal and transverse optical modes.

5. Conclusions

We studied the GHS of both acoustic and optical vibrational modes in the $^{74}\text{Ge}-^{70}\text{Ge}-^{74}\text{Ge}$ structure. Our numerical results highlight the significant dependence of the GHS on the incident angle, the size of the system, and the wavelength of the incident vibrational mode. An interesting feature of the GHS for acoustic vibrations is that for large angles of incidence (greater than 84°) Δy_L^r is approximately equal to Δy_L^t , for all the wavelengths considered. However, for lower angles, Δy_L^r and Δy_L^t are equal only for certain values of the incident wavelength, λ_c . This characteristic wavelength determines the range of wavelengths at which the GHS for reflected modes is greater or less than the GHS for transmitted modes. In the case of transverse optical modes, the transmitted GHS is greater than the reflected one for all incidence angles in the entire wavelength range considered. Furthermore, in general, it is observed that increasing the angle of incidence increases the GHS for both the transmitted and reflected modes; however, there is a range of wavelengths where the GHS decreases with increasing the incidence angle, which is associated with the coupling of the L and T modes. On the other hand, in the case of longitudinal optical modes, an approximately equal GHS is observed for transmitted and reflected waves, as a

consequence of an approximately constant phase difference between them. This result is similar to that reported previously in [8] for SH-modes. It is worth noting that the incident angle not only affects the behaviour of the modes but also influences the magnitude of the GHS. Additionally, the magnitude of the GHS for optical and acoustic modes can exceed several times the incident wavelength or the system length obtaining giant GHS. These findings demonstrate the capacity of this type of systems that, taking advantage of the Goos–Hänchen effect, could be used to design acoustic devices. The properties of vibrational modes studied in this work may be relevant for future research on phonon transport properties in semiconductor heterostructures.

Data availability statement

All data that support the findings of this study are included within the article (and any supplementary files).

Acknowledgments

D Villegas acknowledge the hospitality of Benemérita Universidad Autónoma de Puebla, México. This research was

partially supported by VIEP-BUAP, and Conacyt, México under Grant A1-S23120.

ORCID iDs

Zorayda Lazcano  <https://orcid.org/0000-0003-2970-1268>

Jesús Arriaga  <https://orcid.org/0000-0002-7158-0255>

R Pérez-Álvarez  <https://orcid.org/0000-0003-1119-1159>

Fernando de León-Pérez  <https://orcid.org/0000-0003-0381-3448>

References

- [1] Goos F and Hänchen H 1947 Ein neuer und fundamentaler Versuch zur Totalreflexion *Ann. Phys., Lpz.* **436** 333
- [2] Xu D, He S, Zhou J, Chen S, Wen S and Luo H 2020 Goos-Hänchen effect enabled optical differential operation and image edge detection *Appl. Phys. Lett.* **116** 211103
- [3] Wan Y, Cheng M, Zheng Z and Liu K 2019 Polarization-Modulated, Goos-Hänchen shift sensing for common mode drift suppression *Sensors* **19** 2088
- [4] Guo Y, Singh N M, Das C M, Ouyang Q, Kang L, Li K, Coquet P and Yong K-T 2020 Two-dimensional PtSe₂ theoretically enhanced Goos-Hänchen shift sensitive plasmonic biosensors *Plasmonics* **15** 1815–26
- [5] Han L, Pan J, Wu C, Li K, Ding H, Ji Q, Yang M, Wang J, Zhang H and Huang T 2020 Giant Goos-Hänchen shifts in Au-ITO-TMDCs-graphene heterostructure and its potential for high performance sensor *Sensors* **20** 1028
- [6] Benam E R, Sahrai M and Bonab J P 2020 High sensitive label-free optical sensor based on Goos-Hänchen effect by the single chirped laser pulse *Sci. Rep.* **10** 17176
- [7] Liu Z, Lu F, Jiang L, Lin W and Zheng Z 2021 Tunable Goos-Hänchen shift surface plasmon resonance sensor based on graphene-hBN heterostructure *Biosensors* **11** 201
- [8] Villegas D, Arriaga J, de León-Pérez F and Pérez-Álvarez R 2017 Goos-Hänchen effect for optical vibrational modes in a semiconductor structure *J. Phys.: Condens. Matter* **29** 125301
- [9] Wu J, Wu F, Lv K, Guo Z, Jiang H, Sun Y, Li Y and Chen H 2020 Giant Goos-Hänchen shift with a high reflectance assisted by interface states in photonic heterostructures *Phys. Rev. A* **101** 053838
- [10] Wan R-G and Zubairy M S 2020 Tunable and enhanced Goos-Hänchen shift via surface plasmon resonance assisted by a coherent medium *Opt. Express* **5** 6036
- [11] Zheng Z, Zhu Y, Duan J, Qin M, Wu F and Xiao S 2021 Enhancing Goos-Hänchen shift based on magnetic dipole quasi-bound states in the continuum in all-dielectric metasurfaces *Opt. Express* **29** 29541
- [12] Sreekanth K V, Ouyang Q, Han S, Yong K-T and Singh R 2018 Giant enhancement in Goos-Hänchen shift at the singular phase of a nanophotonic cavity *Appl. Phys. Lett.* **112** 161109
- [13] Saito H, Neo Y, Matsumoto T and Tomita M 2019 Giant and highly reflective Goos-Hänchen shift in a metal-dielectric multilayer Fano structure *Opt. Express* **20** 28629
- [14] Petrov N I, Danilov V A, Popov V V and Usievich B A 2020 Large positive and negative Goos-Hänchen shifts near the surface plasmon resonance in subwavelength grating *Opt. Express* **5** 7552
- [15] Das C M, Kang L, Hu D, Guang Y, Guo Y, Chen M W, Coquet P and Yong K-T 2021 Graphene-coated gold chips for enhanced Goos-Hänchen shift plasmonic sensing *Phys. Status Solidi a* **218** 2000690
- [16] Ma H, Ju C, Ci X and Wu R-X 2020 Nonreciprocal Goos-Hänchen shift by topological edge states of a magnetic photonic crystal *Opt. Express* **28** 19917
- [17] Ma H, Liu M, Wen L, Li Q, Chen H and Yi X 2021 Goos-Hänchen shift in silicene *Results Phys.* **20** 103752
- [18] Zeng L, Dai C and Yin W 2009 Trapped phonon in acoustic metamaterial *Mod. Phys. Lett. B* **23** 2853
- [19] FuPing L, XianJun M, JiaQi X, AnLing W and ChangChun Y 2012 The Goos-Hänchen shift of wide-angle seismic reflection wave *Sci. China Earth Sci.* **55** 852
- [20] de Leo S and Kraus R K 2018 Incidence angles maximizing the Goos-Hänchen shift in seismic data analysis *Pure Appl. Geophys.* **175** 2023
- [21] Fa L et al 2017 Acoustic Goos-Hänchen effect *Sci. China Phys. Mech. Astron.* **10** 104311
- [22] Dadoenkova Y, Dadoenkova N, Krawczyk M and Lyubchanskii I 2018 Goos-Hänchen effect for Brillouin light scattering by acoustic phonons *Opt. Lett.* **43** 16
- [23] Park C M, Yim G-S, Cho K and Lee S H 2020 Hemispherical acoustic Luneburg lens with the acoustic Goos-Hänchen shift and Fresnel filtering effect *Sci. Rep.* **10** 18991
- [24] Haller E E 2010 Physics with isotopically controlled semiconductors *Semiconductors* **44** 841
- [25] Hu J, Schiffl S, Vallabhaneni A, Ruan X and Chen Y P 2010 Tuning the thermal conductivity of graphene nanoribbons by edge passivation and isotope engineering: a molecular dynamics study *Appl. Phys. Lett.* **97** 133107
- [26] Issenmann D et al 2016 Ultrafast study of phonon transport in isotopically controlled semiconductor nanostructures *Phys. Status Solidi a* **213** 541–8
- [27] Levy S, Shlimak I, Dressler D H and Lu T 2013 Direct observation of a multiple-peak structure in the Raman spectra of ⁷⁴Ge and ⁷⁰Ge nanocrystals *J. Appl. Phys.* **113** 044312
- [28] Whiteway E, Lee M and Hilke M 2020 Real-space Raman spectroscopy of graphene isotope superlattices *Phys. Rev.* **102** 235429
- [29] Frank O, Dresselhaus M S and Kalbac M 2014 Raman spectroscopy and in Situ Raman spectroelectrochemistry of isotopically engineered graphene systems *Acc. Chem. Res.* **48** 111–8
- [30] Varade V, Haider G, Pirker L, Panda J, Sykora J, Frank O, Kalbac M and Vejpravova J 2023 Sulfur isotope engineering of exciton and lattice dynamics in MoS₂ monolayers *2D Mater.* **10** 025024
- [31] Imamura K, Tanaka Y and Tamura S 2002 Group velocities of phonons in superlattices *Phys. Rev. B* **65** 174301
- [32] Winful H G 2006 Tunneling time, the Hartman effect and superluminality: a proposed resolution of an old paradox *Phys. Rep.* **436** 1
- [33] Trallero-Giner C, Pérez-Álvarez R and García-Moliner F 1998 *Long Wave Polar Modes in Semiconductor Heterostructures* (Elsevier)
- [34] de León-Pérez F and Pérez-Álvarez R 2001 Phonon propagation in nonpolar semiconductor heterostructures *Phys. Rev. B* **63** 245304
- [35] Strocio M A and Dutta M 2004 *Phonons in Nanostructures* (Cambridge University Press)
- [36] Hauge E H, Falck J P and Fjeldly T A 1987 Transmission and reflection times for scattering of wave packets off tunneling barriers *Phys. Rev. B* **36** 4203
- [37] Lazcano Z, Valdés Negrín P L, Villegas D, Arriaga J and Pérez-Álvarez R 2014 Tunneling times of acoustic phonon packets through a distributed Bragg reflector *Nanoscale Res. Lett.* **9** 449
- [38] Ji Q, Yan B, Han L, Wang J, Yang M and Wu C 2020 Theoretical investigation of an enhanced Goos-Hänchen shift sensor based on a BlueP/TMDC/graphene hybrid *Appl. Opt.* **59** 8355